JOURNAL OF AIRCRAFT
Vol. 37, No. 5, September–October 2000

# Optical Measurements of Flutter Mode Shapes

Jakob Kuttenkeuler*
*Kungliga Tekniska Högskolan, SE-100 44 Stockholm, Sweden*

**The usefulness of an optical motion capture system in aeroelastic wind-tunnel testing is investigated. A system consisting of four infrared charge-coupled device cameras, observing flat passive reflecting markers, is installed in a low-speed tunnel to measure flutter mode shapes. Free vibration and aeroelastic measurements are performed on four wing configurations consisting of thin flat orthotropic composite laminates with varying laminate orientation. The laminate orientations are chosen to result in dissimilar flutter mode shapes. The wings are equipped with up to 20 markers, and the motion is sampled at 240 Hz. Quantitative scalar comparisons between analysis and experiments, with respect to both amplitude and phase are done using the modal assurance criterion (MAC). Measurements of mode shapes on free vibrating wings (ground vibration tests), as well as limit-cycle flutter oscillations, show good agreement with numerical results. MAC ratings consistently exceeding 0.96 are achieved. However, it is clearly seen that the agreement is better for free vibration comparisons than for flutter. This is expected considering the higher complexity of the flutter problem. Thus, the cause cannot be attributed exclusively to insufficiencies in the optical system but also to inaccuracies in the modeling. The good quality of the measurements proves the usefulness of such a noncontact positioning system in experimental wind-tunnel testing, not only in the present flutter context, but in a variety of experimental work affected by aeroelastic deformation.**

## I. Introduction

AEROELASTIC deformation, both static and dynamic, is often an integrated part of wind-tunnel testing. Not only experiments where aeroelastic effects are of primary interest but virtually all experiments where elastic deformation originates from the model itself, the model support, or the balance are affected. Such aeroelastic deformation must be considered when, for example, comparing experimental data with computations based on rigid-body assumptions. Regardless of the cause, there often exists a need to quantify these deformations. Means of doing this involve various types of onboard devices, such as inertial sensors and strain gauges, with all their advantages and disadvantages. To avoid flow interactions, the sensors often have to be placed inside the model, which causes difficulties because sufficient access has to be provided both for the sensor itself as well as for the wiring.

The advantages of using an optical noncontact positioning device for deformation measurements are evident, especially when considering the capabilities of measuring the position of several markers simultaneously. Efforts being made in this field, along with a discussion on various types of video photogrammetric techniques, are presented by Burner et al.[1] An example of the use of optical systems for model deformation measurements at NASA is described by Burner.[2] Further examples of commercially available systems used in wind tunnels are the Northern Digitals Optotrak,[3] used by Boeing, and the ProReflex system[4] by Qualisys, used in this investigation. Optical systems especially developed for flight tests also exist, such as those developed by Grumman[5] and NASA.[6]

Among the basic requirements for a multipurpose positioning system to be appealing in wind-tunnel experiments are adaptable mounting, simple calibration procedures, as well as extensive and highly automated data processing. High sampling rate, multimarker capacity, and the possibility to use flat markers are also required. For use in dynamic aeroelastic experiments, such as the present, many markers are needed to capture the mode shapes whereas real-time data access is of less importance. In quasi-static experiments, or other experiments involving control systems, there is often a need for real-time information feedback of the rigid-body degrees of freedom.

Received 27 December 1998; revision received 27 December 1999; accepted for publication 31 January 2000. 

*Lecturer, Department of Aeronautics.

The present ProReflex system is installed in a low-speed wind tunnel at the Department of Aeronautics, Kungliga Tekniska Högskolan (KTH), to serve as a versatile system in various types of experiments. The overall objective is to use the system for tasks ranging from rigid-body angle-of-attack-type measurements, for feedback in control law experiments, to static as well as dynamic model deformation measurements. Among the advantages of the system is the feasibility to use flat passive tape markers, which are punched out from self-bonding sheets. This, in contrast to the use of active markers, enables fast model preparation, no need for wiring, and flexibility in marker positioning.

The present investigation should be regarded as a part of the system validation, where the aim is to confirm its usefulness for capturing flutter mode shapes in dynamic aeroelastic experiments. The investigation is an extension of earlier numerical/experimental work on aeroelasticity by the author, reported in Refs. 7 and 8. Part of the conclusions from these investigations was that the critical flutter speed is predicted accurately for the considered flat composite wings, which justifies the use of these wings in the present investigation. The flutter speed as a function of material orientation was calculated and verified in several experiments in Refs. 7 and 8. It was found that this function includes a discontinuous derivative as well as being discontinuous itself. The cause of both these occurrences is transitions in critical flutter modes, or eigenvalues. Although capabilities to visualize the calculated mode shapes existed, at the time there existed no efficient means to capture experimentally the motion. The scope of this investigation is therefore to complement the earlier work with comparisons of mode shapes, or eigenvectors, on wings with various laminate orientation.

## II. Experimental Setup

All experiments are performed in a low-speed, closed-return wind tunnel at the Department of Aeronautics, KTH. A symmetric model made of two epoxy-impregnated glass fiber wing halves is clamped horizontally on a sting. The wing geometry and mounting are shown in Fig. 1.

Four geometrically identical wing configurations are investigated. The configurations differ only in that the orientation $\theta$ of the orthotropic glass fiber composite is altered. The setup is identical to the setup in Refs. 7 and 8, with the addition of the optical three-dimensional motion capture system ProReflex.[4] Flat tape markers with diameters of 7–11 mm are used. Marker locations and numbering are shown in Fig. 1.

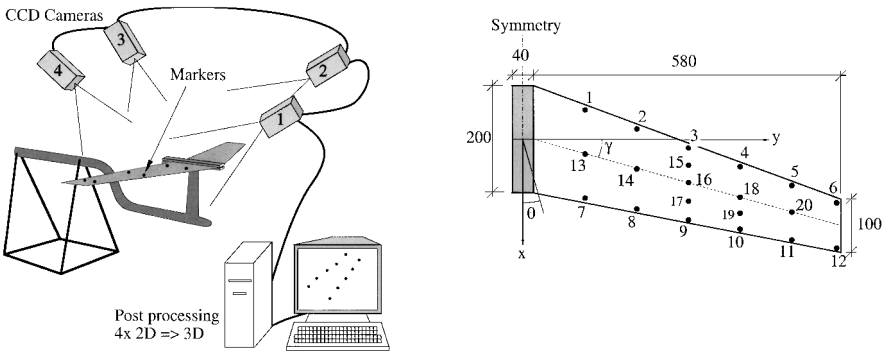


**Fig. 1 Experimental setup showing camera configuration, wing geometry, and numbering of the reflecting markers.**

The ProReflex system in the current setup consists of a host computer and four infrared charge-coupled device (CCD) cameras with internal flashes, each acquiring the optical midpoint of the reflecting markers. Each camera calculates the two-dimensional positions of all visible markers in the plane parallel to its lens. The two-dimensional positions from each camera, in its individual two-dimensional coordinate system, are fed to the host computer where the three-dimensional photogrammetric calculations are performed.

The cameras are mounted in structural parts of the ceiling of the surrounding building to achieve a rigid camera support. Openings, 130 × 130 mm, are cut in the tunnel ceiling to accomplish free camera sight. These openings are left uncovered to avoid optical refraction. The distances between the cameras and the markers are between 1.3 and 1.5 m, and all cameras are focused to cover the same wing-half.

## III. Performance of the Optical Measurement System

The performance of the positioning system depends on several factors. These can roughly be divided into two separate categories, system-dependent factors and factors related to the specific configuration. Examples of system-dependent limitations are the maximum camera sampling rate (here 240 Hz) and the maximum number of markers that the system can handle given a specific sampling rate. Within the second category, the perhaps most significant example is the camera constellation, which strongly affects the precision in three dimensions. A constellation resulting in good stereoscopic separation is naturally desirable. The size and shape of the markers, along with the calibration quality, also affect the accuracy and the resolution. A more thorough discussion on the subject is certainly relevant, but beyond the scope of this report.

A set of static measurements is performed, with $u = 0$, exclusively to measure and verify the precision of the three-dimensional positions obtained using the present configuration. The measurements are done using the experimental setup shown in Fig. 1, but are modified with extra support of the wing to achieve a straight and stationary condition.

Experimentally, based on 50,000 samples, the one-dimensional spatial resolution is found to be approximately 0.03 mm in all three coordinate directions. Typically, the three-dimensional scatter is on the order of ±0.1 mm. Measurements on markers attached to the model support rig during wind-on conditions show similar results, which verifies the rigidity of the camera mounting. The general conclusion is that the measurement accuracy is sufficient but that the limitations have to be considered when evaluating small-amplitude motions.

## IV. Numerical Modeling and Analysis

The orthotropic material properties for the four wing configurations, given in Table 1, are obtained using the modal method described in Ref. 9. The configurations are hereafter referred to using their laminate angle $\theta$, defined in Fig. 1.

All numerical modeling is performed using a finite element based plate description of the wing with Mindlin-type heterosis elements.[10] The mesh consists of 6 elements chordwise and 12 spanwise. The wing root is considered clamped, and internal damping is neglected. The free-vibration motion of the cantilever wing is obtained by solving the eigenvalue problem

$$[\boldsymbol{K} - \omega^2 \boldsymbol{M}]\hat{\boldsymbol{v}} = 0 \tag{1}$$

where $\boldsymbol{K}$ is the stiffness matrix, $\boldsymbol{M}$ the consistent mass matrix, $\omega$ the free-vibration frequency, and $\hat{\boldsymbol{v}}$ the vector of nodal displacements in the finite element model.

For the flutter calculations, the linearized equations of motion for a thin wing in potential flow are written in discretized form as

$$[\boldsymbol{M}\ddot{\boldsymbol{v}} + \boldsymbol{K}\boldsymbol{v}] = \boldsymbol{f}(t) \tag{2}$$

where $\boldsymbol{f}(t)$ is the time-dependent vector of aerodynamic forces. Assuming incompressible linear unsteady aerodynamics and transforming the equations of motion to the frequency domain give the nonlinear eigenvalue problem

$$[p^2\boldsymbol{M} + \boldsymbol{K} - q\boldsymbol{A}(p)]\hat{\boldsymbol{v}} = 0 \tag{3}$$

where $p$ is the eigenvalue, $q$ the dynamic pressure, $\boldsymbol{A}$ the matrix of aerodynamic forces, and $\hat{\boldsymbol{v}}$ the eigenvector. By following of standard procedure,[11] the lowest free-vibration frequencies and corresponding eigenmodes from the linear dynamics finite element model are used to define a smaller subspace. The flutter analysis problem is solved by expressing stiffness, mass, and aerodynamic forces in this smaller subspace. Normalizing the eigenvectors so that the generalized mass is one and assuming that $\boldsymbol{A}$ only depends on the reduced frequency $k = \omega b/u$ give

$$[p^2\boldsymbol{I} + \boldsymbol{\Omega}^2 - q\tilde{\boldsymbol{A}}(k)]\hat{\boldsymbol{w}} = 0 \tag{4}$$

where $\boldsymbol{\Omega}$ is diagonal with a number of free-vibration frequencies on the diagonal, $u$ the airspeed, $\tilde{\boldsymbol{A}}$ the aerodynamic forces expressed in the smaller subspace, $\hat{\boldsymbol{w}}$ the corresponding eigenvector, and $b$ the semichord. The matrix of aerodynamic forces is computed using the doublet-lattice method.[12] The eigenvalues $p$ are found for each flight condition $u$, using a modified version of the $p$–$k$ method.[13] The structure is considered stable for the flight condition if all of the eigenvalues $p$ have negative real part. Earlier work[7,8] has shown good agreement between experimental and numerical results regarding flutter velocity, using the described methodology and material properties.

**Table 1 Material properties of the four wing configurations**

| $\theta$, deg | Thickness, mm | Density, kg/m$^3$ | $D_{11}$,[a] N·m | $D_{12}$,[a] N·m | $D_{22}$,[a] N·m | $D_{33}$,[a] N·m |
|---|---|---|---|---|---|---|
| 0 | 1.97 | 1971 | 18.2 | 2.79 | 16.4 | 3.80 |
| 20 | 2.06 | 1929 | 20.0 | 3.19 | 18.2 | 4.23 |
| 45 | 1.95 | 1978 | 18.1 | 2.84 | 16.4 | 3.76 |
| 70 | 2.06 | 1929 | 20.0 | 3.19 | 18.2 | 4.23 |

[a]Conventional orthotropic plate stiffnesses.

The eigenvector $\hat{\boldsymbol{v}}$ corresponding to the critical eigenvalue describes the predicted flutter mode shape in terms of nodal displacements. Because the load matrix $\boldsymbol{A}$ is complex, the eigenvector $\hat{\boldsymbol{v}}$ is also complex, describing both amplitude and phase of the motion.

To compare the predicted and measured mode shapes, they both have to be evaluated at the same in-plane coordinates. This is achieved through interpolation of the predicted mode shapes, at locations corresponding to the marker positions, using the finite element basis functions.

## V. Free Vibration

The objective in this section is to compare free-vibration amplitudes, frequencies, and phase between the numerical solutions to Eq. (1) and experimental data. Because the deflections have to be of measurable magnitude in the experiments, only the first eigenmode is considered.

In the experiments, the vibration is excited manually by releasing the wing from a deflected state, approximately 50 mm at the wing tip. For consistency and to allow higher modes to settle, only data points corresponding to tip deflections less than 10 mm are used in the data reduction process. During data reduction, the solution to the equation of motion of a viscously damped free vibration is fitted in a least-square sense to the measured out-of-plane displacement component. Each marker data is processed individually when fitting the time-dependent displacement function $v(t)$, which is expressed as

$$v(t) = v_0 + \hat{v}e^{-\zeta\omega_0 t}\sin\left(\omega_0 t\sqrt{1-\zeta^2} + \varphi_0\right) \tag{5}$$

where $v_0$ is any static contribution, $\hat{v}$ the oscillating amplitude, $\zeta$ the nondimensional damping ratio relative to critical damping, $\omega_0$ the undamped free-vibration angular frequency, $\varphi_0$ the phase shift, and $t$ the time. Typically 20 vibration cycles are used in the fitting procedure, although the results show negligible deviations when fewer cycles are used.

In the analysis, all eigenvalues and eigenvectors, obtained by solving Eq. (1) are real because damping is neglected.[14] Hence, when comparing analysis with experiments, the undamped frequency $\omega_0$ (or $f_0 = \omega_0/2\pi$) and the amplitude $\hat{v}$ from Eq. (5) are used. A commonly used scalar measure for comparisons between mode shapes is the modal assurance criterion (MAC)[15] defined as

$$\mathrm{MAC}(\hat{\boldsymbol{v}}_1, \hat{\boldsymbol{v}}_2) = \frac{\left(\hat{\boldsymbol{v}}_1^{\mathrm{T}}\hat{\boldsymbol{v}}_2\right)^2}{\|\hat{\boldsymbol{v}}_1\|^2\|\hat{\boldsymbol{v}}_2\|^2}, \qquad 0 \le \mathrm{MAC} \le 1 \tag{6}$$

where $\hat{\boldsymbol{v}}_1$ and $\hat{\boldsymbol{v}}_2$ are the two mode shape vectors to compare. The MAC number quantifies the normalized scalar product of the two compared vectors. Thus, perfect correlation renders MAC = 1, and a comparison between two orthogonal modes results in MAC = 0.

From the results of the free-vibration comparisons, presented in Fig. 2 and Table 2, it is clear that both the fundamental eigenfrequencies $f_0$ and the mode shapes numbers correlate well between analysis and experiments. The maximum experimental phase difference $\Delta\varphi_{\max}$ between two markers in one wing of 1.65 deg is also affirmatively low.

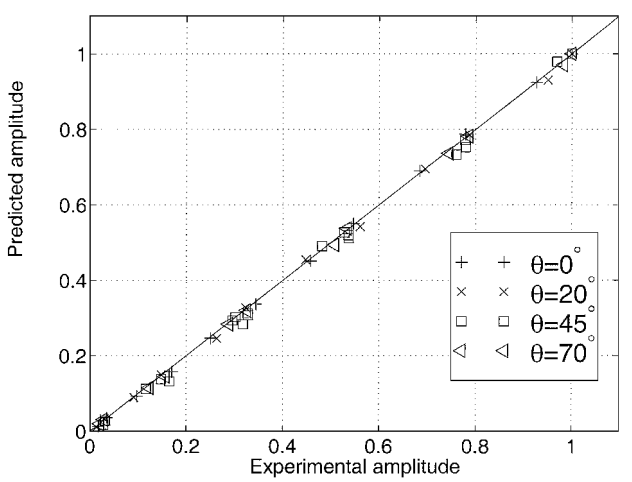


**Fig. 2 Numerical vs experimental free-vibration results at marker positions for all four configurations.**

**Table 2 Free vibration comparisons between predicted and experimental results**

| $\theta$, deg | $f_{0_{\mathrm{pred}}}$, Hz | $f_{0_{\mathrm{exp}}}$, Hz | $\Delta\varphi_{\max}$, deg | MAC ($\hat{\boldsymbol{v}}_{\mathrm{pred}}$, $\hat{\boldsymbol{v}}_{\mathrm{exp}}$) | Markers nos. |
|---|---|---|---|---|---|
| 0 | 3.79 | 3.71 | 0.46 | 1.00 | 1–12 |
| 20 | 3.60 | 3.36 | 1.65 | 1.00 | 1–12 |
| 45 | 3.52 | 3.49 | 1.23 | 1.00 | 1–20 |
| 70 | 4.22 | 4.14 | 1.00 | 1.00 | 1–12 |

**Table 3 Condensed flutter results, both predicted and experimental**

| $\theta$, deg | $u_{\mathrm{pred}}$, m/s | $u_{\mathrm{exp}}$, m/s | $f_{\mathrm{pred}}$, Hz | $f_{\mathrm{exp}}$, Hz | MAC ($\hat{\boldsymbol{v}}_{\mathrm{pred}}$, $\hat{\boldsymbol{v}}_{\mathrm{exp}}$) | Markers nos. |
|---|---|---|---|---|---|---|
| 0 | 36.4 | 36.5 | 14.8 | 15.1 | 0.99 | 1–12 |
| 20 | 45.3 | 43.7 | 15.4 | 14.0 | 1.00 | 1–12 |
| 45 | 47.8 | 47.2 | 23.8 | 24.9 | 0.96 | 1–20 |
| 70 | 41.2 | 41.6 | 16.2 | 15.2 | 1.00 | 1–12 |

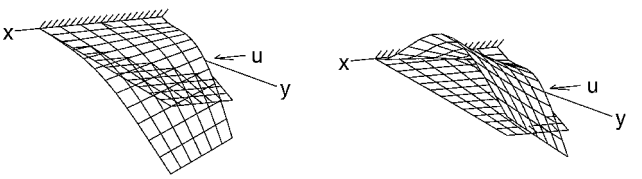


$\theta = 0$ deg wing $\qquad$ $\theta = 45$ deg wing

**Fig. 3 Flutter mode shape superimposed on the nondeflected wing.**

## VI. Flutter

As shown in Ref. 7, the critical flutter speed expressed as a function of laminate orientation has a discontinuous derivative at $\theta = 39$ deg and is itself discontinuous at $\theta = 57$ deg. It was concluded that both occurrences are caused by a stability mode transition. Further comparisons of these different modes reveal that the mode shapes (eigenvectors) for $\theta = 0$, 20, and 70 deg are virtually identical. The MAC ratings of these mode shapes, when comparing the full-length predicted eigenvectors (325 nodes) with each other, are all higher than 0.96. However, the predicted mode shape for $\theta = 45$ deg differs substantially from the others, with a corresponding maximum of MAC = 0.19 when compared with them. The mode shapes for $\theta = 0$ and 45 deg superimposed on the nondeflected wing are shown in Fig. 3.

The flutter experiments are carried out much in the same manner as in Refs. 7 and 8 at an angle of attack just enough to compensate for gravity, hence achieving a straight (nondeflected) wing. At barely subcritical airspeed, the acquisition is initiated, and the airspeed slowly increased stepwise until flutter is visually detected. The data acquisition is continued at constant airspeed to capture the steady-state oscillation at maximum amplitudes of approximately 5 mm. Because the numerical model at best can be expected to be accurate at small flutter amplitudes, it would be ideal to capture experimentally the mode shape at the onset of flutter. However, this is not feasible in practice for reasons of experimental resolution. The experiments and data reduction have to be performed at reasonable flutter amplitudes, as well as at steady-state oscillation.

The postprocessing of the marker data is done in a similar manner to that for the free-vibration tests, that is, by fitting of an harmonic function. However, the damping is now excluded from Eq. (5) due to the nontransient characteristics of the motion. The function is fitted, in a least-square sense, to each marker data covering 6–10 periods. Because, overall, small amplitudes are desired, even at the wing tip, the amplitudes near the wing root approach the experimental resolution, resulting in less confident results in this region.

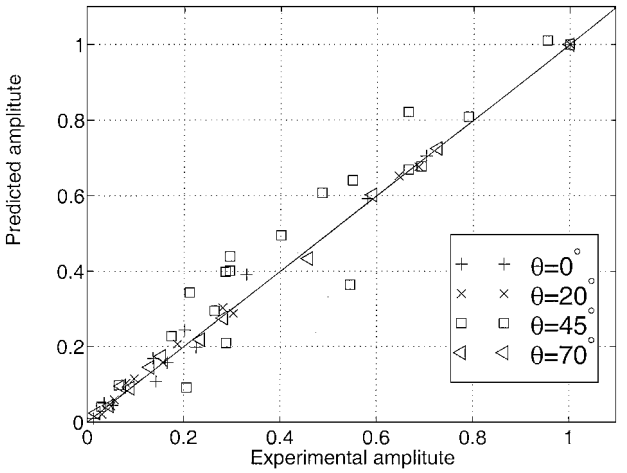


**Fig. 4 Numerical vs experimental flutter amplitudes, at marker positions, for all four configurations.**

Table 3 shows the condensed results from both flutter analysis and experiments. It is found that the critical airspeed, as well as the flutter frequency, is fairly accurately predicted. The maximum discrepancies of about 5% in airspeed and 9% in frequency are here considered good. A visual comparison of the predicted flutter amplitudes vs the experimentally obtained amplitudes in all configurations is shown in Fig. 4. The amplitudes are normalized with the maximum amplitude in the corresponding configuration. It is seen that the agreement is good for the $\theta = 0$-, 20-, and 70-deg configurations but is somewhat more indistinct for $\theta = 45$ deg.

The picture is much the same when considering the phase disagreement between experimental and analytical results. The largest disagreements are found for markers experiencing small, close to the measurement resolution, motion amplitudes. Typically, the disagreement in phase between analysis and experiments are less than 10 deg, which is considered satisfactory.

Although the correlation in Fig. 4 is good, it is observed that the deviations in flutter amplitudes are considerably larger than in the free-vibration comparisons (Fig. 2). Explanations to this are likely found in both the analysis and the experiments. Experimentally, the higher frequencies and lower amplitudes of the flutter motion, compared to the free vibration, increase the measurement errors. The flutter analysis also contributes through uncertainties in the modeling of the unsteady aerodynamic forces. Note that the analysis predicts the dynamics at the onset of flutter whereas the measurements are done at limit-cycle oscillation.

## VII. Conclusions

The ability to measure aeroelastic deformation simultaneously at several locations on a wind-tunnel model without onboard sensors is a significant advantage. Although limited, this investigation shows the potential of such a system. With the use of the present setup of the ProReflex[4] system, a three-dimensional positioning resolution of 0.03 mm and a typical precision of 0.1 mm are achieved during simultaneous sampling of 20 markers at 240 Hz.

Comparisons between predicted and experimentally obtained fundamental free-vibration mode shapes show excellent agreement. Consistent high MAC ratings are achieved for all four investigated wing configurations, and good frequency matching is also attained. These results also verify the modeling of the structural dynamics, as well as the elastic material properties.

The comparisons of flutter mode shapes are somewhat more difficult to interpret. High MAC ratings (MAC $\geq$0.96) between calculations and experiments are again obtained, but a somewhat more thorough comparison reveal differences in phase angle, generally less than 10 deg but occasionally worse. However, the less accurate phase angle correlations correspond to locations (or markers) subject to low oscillation amplitudes, which result in less accurate evaluations of the experimental data.

The two different predicted flutter mode shapes, shown in Fig. 3, are clearly experimentally verified. It is clearly seen that the more complex mode shape (for $\theta = 45$ deg), with small amplitudes and high frequency, results in the largest discrepancies between calculations and experiments. The explanation is most likely found in limitations in both the analysis and the experimental methods.

The main objective here is to evaluate the feasibility of measuring the dynamic behavior of wind-tunnel models. Promising results show that the system is useful, although limitations exist. Some system-dependent limitations, such as sampling frequency and maximum number of markers, are at the lower bound of acceptance. Improvements of the installation, such as in camera constellation and choice of lenses can possibly also improve the measurement quality.

## Acknowledgment

This work was supported by the National Program for Aeronautics Research of the Swedish government.

## References

[1]Burner, A. W., Radeztsky, R. H., and Liu, T., "Videometric Applications in Wind Tunnels," TR 1250, NASA Langley Research Center, Aug. 1997.

[2]Burner, A. W., "Model Deformation Measurements at Nasa Langley Research Center," TR 1202, NASA Langley Research Center, Sept. 1997.

[3]Watzlavick, R. L., Crowder, J. P., and Wright, F. L., "Comparison of Model Attitude Systems: Active Target Photogrammetry, Precision Accelerometer, and Laser Inteferometer," 19th AIAA Advanced Measurement and Ground Testing Technology Conf., AIAA Paper 96-2252, 1996.

[4]ProReflex, Technical Reference, Ver. 6.41, Qualisys AB, Sävedalen, Sweden, 1997.

[5]DeAngelis, V. M., and Fodale, R., "Electro-Optical Flight Deflection Measurement System," Society of Flight Test Engineers Conf., 1987.

[6]Lokos, W. A., "Predicted and Measured In-Flight Wing Deformations of a Forward-Swept-Wing Aircraft," NASA TM 4245, Nov. 1990.

[7]Kuttenkeuler, J., and Ringertz, U., "Aeroelastic Design Optimization with Experimental Verification," *Journal of Aircraft*, Vol. 35, No. 3, 1998, pp. 505–507.

[8]Kuttenkeuler, J., and Ringertz, U., "Aeroelastic Tailoring Considering Uncertainties in Material Properties," *Structural Optimization*, Vol. 15, No. 3, 1998, pp. 157–162.

[9]Kuttenkeuler, J., "A Finite Element Based modal Method for Determination of Plate Stiffnesses Considering Uncertainties," *Journal of Composite Materials*, Vol. 33, No. 8, 1999, pp. 681–772.

[10]Hughes, T. J. R., *The Finite Element Method: Linear Static and Dynamic Finite Element Analysis,* Prentice–Hall, Englewood Cliffs, NJ, 1987, pp. 445–450.

[11]Dowell, E. H., Curtiss, H. C., Scanlan, R. H., and Sisto, F., *A Modern Course in Aeroelasticity*, Kluwer, Dordrecht, The Netherlands, 1989, pp. 129–157.

[12]Albano, E., and Rodden, W. P., "A Doublet-Lattice Method for Calculating Lift Distributions on Oscillating Surfaces in Subsonic Flows," *AIAA Journal*, Vol. 7, No. 2, 1969, pp. 279–285.

[13]Bäck, P., and Ringertz, U. T., "On the Convergence of Methods for Nonlinear Eigenvalue Problems," *AIAA Journal*, Vol. 35, No. 6, 1997, pp. 1084–1087.

[14]Friswell, M. I., and Mottershead, J. E., *Finite Element Model Updating in Structural Dynamics*, Kluwer, Dordrecht, The Netherlands, 1996, pp. 13–24.

[15]Ewins, D. J., *Modal Testing: Theory and Practice*, Research Studies, Somerset, England, U.K., 1994, pp. 224–226.